Computational Mechanics
https://doi.org/10.1007/s00466-018-1629-y

ORIGINAL PAPER

Electrodynamic machine-learning-enhanced fault-tolerance of robotic free-form printing of complex mixtures

T. I. Zohdi[1]

Received: 25 May 2018 / Accepted: 25 August 2018

Abstract
Rapid free-form printing of particle-functionalized materials is an integral component of 3D printing and additive manufacturing. Such processes consist of attaching a dispenser to a robot arm which then releases droplets of specialized mixtures in free-space that are deposited onto a substrate. These approaches are popular because they utilize widely-available, highly-programmable, robots. However, often the release of a complex mixture in free-space is somewhat imprecise, thus electrodynamic field control has been proposed as a possible remedy to enhance the precision of such processes. Specifically, electrodynamic control of the material is achieved by electrifying the released material in the presence of a prescribed ambient electrical field generated from the substrate, in order to guide it to the desired position. There are many components that comprise such a system, thus motivating the construction of a simulation tool framework assembling submodels of the:

- kinematics of the robot arm and the dispenser-printer head,
- electrodynamic and gravitational forces on the released material,
- dynamics of the released material and
- conductive, convective and radiative cooling of the media.

The modular system structure allows for easy replacement of submodels within the overall framework. Numerical simulations are undertaken to illustrate the overall system model, which is comprised of an assembly of submodels. Afterwards, a Machine Learning Algorithm (MLA) is developed to identify and optimize the proper system parameters which deliver a desired printed pattern. Specifically, an MLA is developed to ascertain the appropriate combination of robotic motion and electrical fields needed to create structures which would be difficult or impossible by purely mechanical means alone. Afterwards, extensions involving more detailed models are then provided, based on the Discrete Element Method.

Keywords Printing · Electrodynamics · Simulation

1 Introduction

As the rapid digitalization of industry has been taking place, manufacturers have been scrambling to meld simulation software with emerging technologies based on embedded sensor technology, autonomous robotics, virtual reality (VR) and artificial intelligence (AI). Integrated advanced sensors, controls, simulation platforms and modeling has made next-generation advanced manufacturing, sometimes referred to as Industry 4.0, possible (Zohdi and Dornfeld [1] and Huang et al [2]). For the purposes of this paper, we refer to this entire evolving area as "Advanced Manufacturing". Advanced Manufacturing requires the development of models and simulation tools that can be run rapidly for design purposes, which then naturally lend themselves to optimization strategies such as Machine Learning Algorithms (MLAs), which require several hundred or thousand simulation runs during in an extremely short period of time.

Specialized MLAs, digital twin technology and complex materials are key factors in these processes, which have now become critical to industrialized economies. It is estimated that digitized manufacturing will generate $1 trillion in net global value over the next four years by streamlining design,

✉ T. I. Zohdi
zohdi@me.berkeley.edu

[1] Department of Mechanical Engineering, University of California, Berkeley, CA 94720-1740, USA

Published online: 11 September 2018

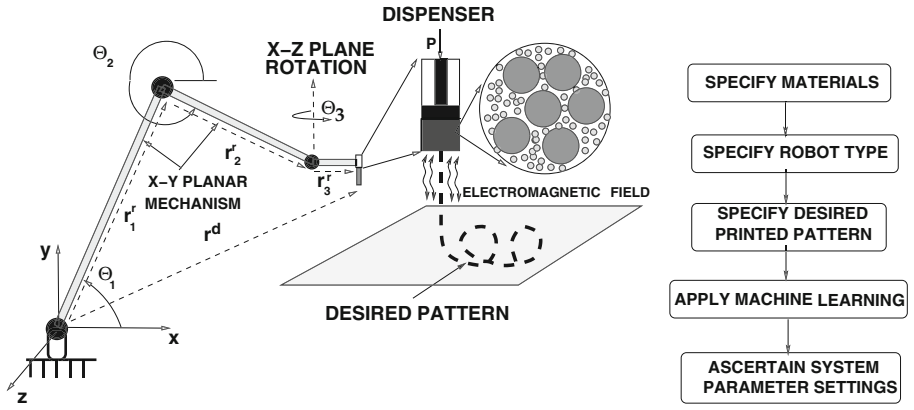

Fig. 1 Model problem of a robot with a dispensing printer head

manufacturing processes and managing supply chain risks. One type of paradigm that is useful to determine the parameters needed for multicomponent systems to properly function is Machine Learning, which has now really become critical for all forms of advanced manufacturing, such as 3D printing. A particular type of 3D printing that is becoming popular is free-form printing, which is comprised of a multi-axis robot arm equipped with a dispenser that dispenses droplets of specialized mixtures. However, this type of process has many design parameters. These approaches are popular because they utilize widely-available highly-programmable robots that have been developed for decades in other fields. However, often the release of a complex mixture in free-space is somewhat imprecise, thus electrical field control has been proposed as one possible remedy to enhance the precision of such processes. Specifically, electrical control of the material is achieved by electrifying the released material in the presence of a prescribed electric field generated on the substrate, in order to guide it to the desired position. There are many components that comprise such a system, thus motivating the construction of a simulation tool framework in this paper assembling submodels of:

- The kinematics of the robot arm and the dispenser-printer head,
- The electrodynamic and gravitational forces on the released material,
- The dynamics of the released material and
- The conductive, convective and radiative cooling of the media.

The modular system structure allows for easy replacement of submodels within the overall framework. In this work, numerical simulations are undertaken to illustrate the overall system model, which is comprised of an assembly of submodels. An MLA is then developed to identify and optimize the proper system parameters which deliver a desired printed pattern. Specifically, an MLA is developed to ascertain the appropriate combination of robotic motion and electric fields needed to create structures which would be difficult or impossible by purely mechanical means alone. Afterwards, extensions using more detailed models are then provided, based on the Discrete Element Method.

2 A model problem: free-form robotic printer

As a model problem, (Fig. 1), we consider a robot linkage, with a mounted dispenser, described via vector loops which are widely used in the robotics literature (for example, see Hunt [3], Hartenberg and Denavit [4], Howell [5], McCarthy [6], [7], Reuleaux [8], Sandor and Erdman [9], Slocum [10], Suh and Radcliffe [11] and Uicker et al. [12]). Links one and two are x–y planar, while link three is in the x–z plane. We assume that we can precisely control the angles and angular velocities of all of the links in the system. The position vector ($\boldsymbol{r}^d$) to the dispenser is given by

$$\boldsymbol{r}^d = \boldsymbol{r}_1^r + \boldsymbol{r}_2^r + \boldsymbol{r}_3^r. \tag{1}$$

Differentiating, a velocity vector loop is generated

$$\boldsymbol{v}^d = \dot{\boldsymbol{r}}_1^r + \dot{\boldsymbol{r}}_2^r + \dot{\boldsymbol{r}}_3^r = \dot{\boldsymbol{r}}^d. \tag{2}$$

In component form, for the x components of position

$$r_x^d = r_1^r cos\Theta_1 + r_2^r cos\Theta_2 + r_3^r sin\Theta_3, \tag{3}$$

for the y components of position

$$r_y^d = r_1^r sin\Theta_1 + r_2^r sin\Theta_2 \tag{4}$$

and for the z components of position

$$r_z^d = r_3^r cos\Theta_3, \tag{5}$$

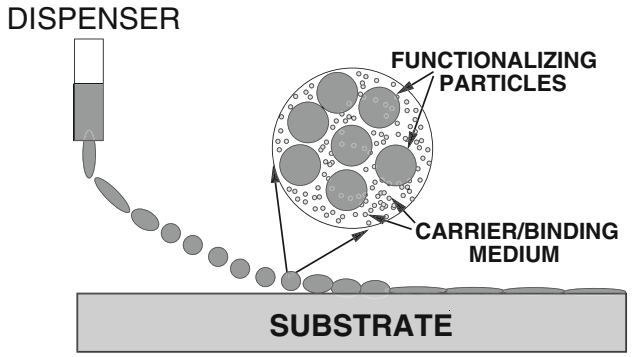

Fig. 2 Deposition of "droplets" of a mixtures

where the link lengths are given by $r_i^r = ||\boldsymbol{r}_i^r|| = \sqrt{\boldsymbol{r}_i^r \cdot \boldsymbol{r}_i^r}$ (for $i = 1, 2, 3$) and the planar (x–y) angles are measured counter-clockwise from horizontal right (Fig. 1). The velocities can subsequently found from differentiating the component equations of Eqs. 3–16, yielding, for the x components of velocity

$$v_x^d = -r_1^r \dot{\Theta}_1 sin\Theta_1 - r_2^r \dot{\Theta}_2 sin\Theta_2 + r_3^r \dot{\Theta}_3 cos\Theta_3, \tag{6}$$

for the y components of velocity,

$$v_y^d = r_1^r \dot{\Theta}_1 cos\Theta_1 + r_2^r \dot{\Theta}_2 cos\Theta_2 \tag{7}$$

and for the z components of velocity

$$v_z^d = -r_3^r \dot{\Theta}_3 sin\Theta_3. \tag{8}$$

The total velocity of the droplet coming out of the dispenser is the velocity of the dispenser plus the relative droplet dispenser velocity ($\Delta \boldsymbol{v}^e$):

$$\boldsymbol{v} = \boldsymbol{v}^e + (\boldsymbol{v} - \boldsymbol{v}^e) = \boldsymbol{v}^e + \Delta \boldsymbol{v}^e. \tag{9}$$

3 Dynamics of released material

The dispensed material, which is released as "syrup-like" droplets of multiphase mixtures as the robotic system moves (Fig. 2), is represented by a series of lumped masses. Macroparticle interaction within the droplet mixture, as well as the interaction between the droplets of mixtures are not considered in this part of the analysis, since this is not relevant for the overall macroscale robot path planning calculations of the printing process. However, detailed modeling of the dynamics of the released material is discussed later in the paper.

Accordingly, for the lumped mass analysis, at a snapshot in time, and an arbitrary ith lumped mass in the system, whose dynamics are governed by

$$m_i \ddot{\boldsymbol{r}}_i = \boldsymbol{\Psi}_i^{elec} + \boldsymbol{\Psi}_i^{grav} + other\ external\ forces \stackrel{\text{def}}{=} \boldsymbol{\Psi}_i^{tot}(\boldsymbol{r}_1, \boldsymbol{r}_2, ..., \boldsymbol{r}_{N_m}), \tag{10}$$

where $\boldsymbol{r}_i$ is the position vector of the ith lumped mass, $\boldsymbol{\Psi}^{elec}$ are the externally applied electrical force, $\boldsymbol{\Psi}_i^{grav} = m_i \boldsymbol{g}$ is the gravitational force and $\boldsymbol{\Psi}_i^{tot}$ is the total of the forces acting on the ith lumped mass.

Remark Often when a complex fluidized mixture exits a dispenser, a droplet is formed. However, it can initially exit as a long slender filament, that will break up into droplets, due to instabilities. The breakup of a long column of fluid from a dispenser, possessneting slight perturbations (longitudinal waviness) was first experimentally studied by Plateau in 1873, who determined that a vertically falling water stream into drops if its wavelength is greater than approximately 3.13–3.18 times its diameter. Subsequently, Rayleigh analytically proved that a wavy falling column of liquid (with circular cross-section) will break up into drops if its wavelength exceeded its circumference. This type of instability is driven by surface tension, which forces fluids to minimize their surface area. See Papageorgiou [13] and Eggers [14] for more details. In the case of a dispensed viscous medium, the degree of fluidity/viscosity influences surface tension. We refer the reader to Zohdi [15] for detailed simulation of this phenomena. In the present analysis, we assume that the droplet has been formed. Later in the paper this stream/droplet phenomenon is discussed further.

4 Construction of targeted electrified field

A key in digital printing is the targeted zonal electrification of the substrate to guide the material to the precise desired locations. This is done, as in the classical "xerox" process by charging pixels on the substrate, turning them on and off in a controlled manner, to attract the deposited material to key locations. To construct an electrified pattern, consider an electric field due to charged external point source, representing one pixel on the substrate (Fig. 3), which is governed by Gauss' law:

$$\int_A \boldsymbol{D} \cdot \boldsymbol{n}\, dA = \epsilon E 4\pi ||\boldsymbol{r} - \boldsymbol{r}_o||^2 = \int_V Q_c\, dV = q_p \Rightarrow \boldsymbol{E} = \frac{q_p}{4\pi\epsilon ||\boldsymbol{r} - \boldsymbol{r}_o||^2}\boldsymbol{n}, \tag{11}$$

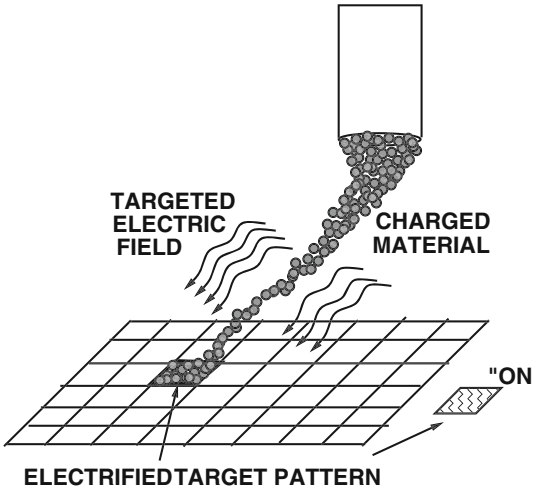

Fig. 3 Highly targeted feature patterns that are electrified

where $\boldsymbol{D}$ is the electric field flux, $\boldsymbol{E}$ is the electric field ($E = \pm||\boldsymbol{E}||$), Q_c is the charge per unit volume, q_p is the total charge at the point source, $\boldsymbol{n}$ is the normal-outward unit vector and $||\boldsymbol{r} - \boldsymbol{r}_o||$ is the distance from the point source. To create the electric field associate with the entire set of pixels, one simply superposes the individual fields. Thus, using the point sources, the process is:

1. *Activation of point sources*

$$\boldsymbol{E}_p = \frac{q_p}{4\pi\epsilon||\boldsymbol{r}_i - \boldsymbol{r}_p||^2}\boldsymbol{n}_{i\to p}. \tag{12}$$

2. *Construction of induced e-field:*

$$\boldsymbol{E}^{ext}(\boldsymbol{r}_i) = \sum_{p=1}^{N_c} \frac{q_p}{4\pi\epsilon||\boldsymbol{r}_i - \boldsymbol{r}_p||^2}\boldsymbol{n}_{i\to p}, \tag{13}$$

where N_c are the number of charged point sources. The induced electrical force on the released material is $\boldsymbol{\Psi}_i^{elec} = q_i\boldsymbol{E}^{ext}(\boldsymbol{r}_i)$, where q_i is the charge of released material and $\boldsymbol{E}^{ext}$ is the electrical field constructed by the points on the substrate.

Remark A general electromagnetic field (as opposed to the previous purely electrical field) can be introduced in two parts: (1) Lorentz forces (for charged/electrified materials) and (2) magnetic forces (for magnetic materials). In mathematical form,

$$\boldsymbol{\Psi}_i^{e+m} = \boldsymbol{\Psi}_i^{lor,e+m} + \boldsymbol{\Psi}_i^{mag} = \underbrace{q_i(\boldsymbol{E}^{ext} + \boldsymbol{v}_i \times \boldsymbol{B}^{ext})}_{\boldsymbol{\Psi}_i^{lor,e+m}} + \boldsymbol{\Psi}_i^{mag}, \tag{14}$$

where Lorentz-induced forces from independent external fields are $\boldsymbol{E}^{ext}$ and $\boldsymbol{B}^{ext}$ is $\boldsymbol{\Psi}_i^{lor,e+m}$. The terms $\boldsymbol{E}^{ext}$ and $\boldsymbol{B}^{ext}$ are considered to be externally controlled and uncoupled from one another (Jackson [17]). In addition to using electrical fields to guide material to the target location, electrical fields may be needed help extract the highly viscous particle-laden material complex from the dispenser. Although this issue is not simulated here, we refer the reader to Zohdi [16] for more details.

5 Drag forces

Because the process could be in an open air environment, drag effects can be relevant. For example, we will employ a general phenomenological model

$$\boldsymbol{\Psi}_i^{drag} = \frac{1}{2}\rho_a C_{Di}||\boldsymbol{v}^f - \boldsymbol{v}_i||(\boldsymbol{v}^f - \boldsymbol{v}_i)A_i^D, \tag{15}$$

where C_{D_i} is the drag coefficient, A_i^D is the reference area, which for a sphere is $A_i^D = \pi R_i^2$, ρ_a is the density of the ambient fluid environment and $\boldsymbol{v}^f$ is the velocity of the surrounding medium which, in the case of interest, is air which is included in the equation of motion for the ith droplet in the system

$$m_i\dot{\boldsymbol{v}}_i = \boldsymbol{\Psi}_i^{tot} = \boldsymbol{\Psi}_i^{elec} + \boldsymbol{\Psi}_i^{grav} + \boldsymbol{\Psi}_i^{drag}. \tag{16}$$

The empirical drag coefficient varies with Reynolds number. For example, consider the following piecewise relation (Chow [18]):

- For $0 < Re \leq 1$, $C_{Di} = \frac{24}{Re}$,
- For $1 < Re \leq 400$, $C_{Di} = \frac{24}{Re^{0.646}}$,
- For $400 < Re \leq 3\times 10^5$, $C_{Di} = 0.5$,
- For $3\times 10^5 < Re \leq 2\times 10^6$, $C_{Di} = 0.000366Re^{0.4275}$,
- For $2\times 10^6 < Re < \infty$, $C_{Di} = 0.18$,

where the local Reynolds number for a drop is $Re \overset{\text{def}}{=} \frac{2R\rho_a||\boldsymbol{v}^f - \boldsymbol{v}_i||}{\mu_f}$ and μ_f is the fluid viscosity.[1] We note that in the zero Reynolds number limit the drag is Stokesian. Using the piecewise relation reduces the drag at the lower Reynolds number regimes.

Remark The piecewise drag law of Chow [18] is a mathematical description for the Reynolds number over a wide range and is a curve-fit of extensive data from Schlichting [98].

[1] The viscosity coefficient for air is $\mu_f = 0.000018$ Pa/s.

6 Heat transfer

For the thermodynamics of lumped masses/drop, we consider conduction, convection and radiation. Thus, for each lumped mass/drop ($i = 1, 2, ..., N_d$),

$$m_i C_i \dot{\theta}_i = \mathcal{Q}_i + \mathcal{H}_{ci} + \mathcal{H}_{ri} + \mathcal{H}_{di}, \tag{17}$$

where θ_i is the temperature in degrees Kelvin, C_i is the heat capacity per unit mass, $\mathcal{Q}_i$ represents the conductive contribution from the substrate, when in makes contact, the robotic dispenser and support structures (if any), $\mathcal{H}_{ci}$ represents surrounding convection, $\mathcal{H}_{ri}$ represents the (infrared) radiation and $\mathcal{H}_{di}$ represents the drag heating. It is assumed that the temperature fields are uniform within the (small) elements surrounding the lumped masses. This assumption is justified, i.e. a lumped thermal model (associates with the lumped masses), ignoring temperature gradients and assuming a uniform temperature when the Biot number is small. The Biot number for a cylindrical element scales with the ratio of the element volume (V) to the element surface area (A^s), $\frac{V}{A^s} = \frac{4\pi R^3/3}{4\pi R^2} = \frac{R}{3}$ (R is the radius of the droplet), which indicates that a uniform temperature distribution is appropriate, since the elements, by definition, are small. Assuming that the fields are uniform in each element allows for the following (for the $i = 1, 2, ..., N_d$ lumped masses)

$$\mathcal{Q}_i \approx I\!K_i \frac{\theta_{sub} - \theta_i}{||\boldsymbol{r}_i - \boldsymbol{r}_{sub}||} A_i^c, \tag{18}$$

where $I\!K_i$ is the conductivity, θ_{sub} is the temperature of the substrate, $\boldsymbol{r}_{sub}$ is the position of the substrate and $A_i^c = \pi R_i^2$ is the contact area associated with the lumped mass/substrate pair (ij). This yields, including standard convection and radiation terms

$$\begin{aligned} m_i C_i \frac{d\theta_i}{dt} = & \underbrace{I\!K_i \frac{\theta_{sub} - \theta_i}{||\boldsymbol{r}_i - \boldsymbol{r}_{sub}||} A_i^c}_{\mathcal{Q}_i\,(when\ in\ contact)} - \underbrace{h_i A_i^s (\theta_i - \theta_s)}_{\mathcal{H}_{ci}} \\ & - \underbrace{\epsilon_i \beta A_i^s (\theta_i^4 - \theta_s^4)}_{\mathcal{H}_{ri}}, \end{aligned} \tag{19}$$

where h_i is the convection coefficient, $A^s \approx 4\pi R^2, 0 \leq \epsilon_i \leq 1$ is the radiative efficiency and $\beta = 5.67 \times 10^{-8} \mathrm{W/(m^2 K^4)}$ is the Stefan–Boltzmann constant. Upon contact the drop is assumed to stick and collapse into a roughly cylindrical shape with the following areas: (a) substrate contact area=πR^2 (b) convective area=$\pi R^2 + 2\pi RL$, where L is determined by the equating the volume of material in the spherical state to the cylindrical configuration ($\pi R^2 L = 4\pi R^3/3$) that is exposed and (c) radiative area= $\pi R^2 + 2\pi RL$ (neglecting the radiative exchange with the substrate). Finally, although potentially small, for the drag-heating rate, we take the inner-product of the drag force with the relative velocity of the drop to the surrounding environment, and insert it into the First Law of Thermodynamics:

$$\begin{aligned} \mathcal{H}_{di} &= \gamma_i \boldsymbol{\Psi}_i^{drag} \cdot (\boldsymbol{v}^f - \boldsymbol{v}_i) \\ &= \gamma_i \frac{1}{2} \rho_a C_{Di} ||\boldsymbol{v}^f - \boldsymbol{v}_i|| (\boldsymbol{v}^f - \boldsymbol{v}_i) A_i^D \cdot (\boldsymbol{v}^f - \boldsymbol{v}_i) \\ &= \gamma_i \frac{1}{2} \rho_a C_{Di} ||\boldsymbol{v}^f - \boldsymbol{v}_i||^3 A_i^D, \end{aligned} \tag{20}$$

where $0 \leq \gamma_i \leq 1$ is the frictional heating efficiency. If one then includes convective and radiative cooling, this yields

$$\begin{aligned} m_i C_i \dot{\theta}_i = & \underbrace{I\!K_i \frac{\theta_{sub} - \theta_i}{||\boldsymbol{r}_i - \boldsymbol{r}_{sub}||} A_i^c}_{\mathcal{Q}_i\,(when\ in\ contact)} - \underbrace{h_i A_i^s (\theta_i - \theta_s)}_{\mathcal{H}_{ci}} \\ & - \underbrace{\epsilon_i \beta A_i^s (\theta_i^4 - \theta_s^4)}_{\mathcal{H}_{ri}} \\ & + \underbrace{\gamma \frac{1}{2} \rho_a C_{Di} ||\boldsymbol{v}^f - \boldsymbol{v}_i||^3 A_i^D}_{\mathcal{H}_{di}}. \end{aligned} \tag{21}$$

Remark To quantify the convection coefficient (h), we consider the Nusselt number (Nu), which is the ratio between the heat transfer of convection to heat transfer of conduction

$$Nu \stackrel{\text{def}}{=} \frac{hL}{I\!K} \Rightarrow h = \frac{Nu I\!K}{L}, \tag{22}$$

where $L = 2R$ is the length scale associated with the particle radius R and $I\!K$ is the fluid conductivity. The Nusselt number is related to the Reynolds number

$$Re \stackrel{\text{def}}{=} \frac{2\rho R ||\boldsymbol{v}^f - \boldsymbol{v}_i||}{\mu}, \tag{23}$$

and Prandtl number

$$Pr \stackrel{\text{def}}{=} \frac{c_p \mu}{I\!K}, \tag{24}$$

by (Whitaker [20])

$$Nu \approx 2 + (0.4 Re^{1/2} + 0.06 Re^{2/3}) Pr^{0.4} \left(\frac{\mu}{\mu_s}\right)^{0.25}, \tag{25}$$

where μ is the surrounding fluid viscosity at the surrounding and μ_s is the viscosity of the fluid at the surface temperature. Thus, once one has the Nusselt number, one can post-process the convection coefficient.[2]

[2] In the analysis to follow, we assume $\mu \approx \mu_s$.

7 Effective properties

In the analysis to follow, the properties of a droplet, which is a mixture of microheterogeneous materials, will be determined from effective medium theories.

7.1 Effective conductivity

Over the last century, estimates for micro-heterogeneous materials, of which porous materials is a subclass, have been developed. A particularly useful set estimates, in fact rigorous bounds are those developed in the early 1960's by Hashin and Shtrikman [21–23]. For a two phase material, comprised of isotropic phases with an overall isotropic response, they specifically read as

$$\underbrace{I\!K_1 + \frac{v_2}{\frac{1}{I\!K_2 - I\!K_1} + \frac{1-v_2}{3I\!K_1}}}_{I\!K^{*,-}} \leq I\!K^* \leq \underbrace{I\!K_2 + \frac{1-v_2}{\frac{1}{I\!K_1 - I\!K_2} + \frac{v_2}{3I\!K_2}}}_{I\!K^{*,+}}, \tag{26}$$

where the conductivity of phase 2 (with volume fraction v_2) is larger than phase 1 ($I\!K_2 \geq I\!K_1$). For the purposes of this present analysis v_2 corresponds to the solid particle material and phase 1 will be considered as the binding "material". The volume fractions have to sum to unity:

$$v_1 + v_2 = 1 \Rightarrow v_1 = 1 - v_2. \tag{27}$$

The Hashin–Shtrikman bounds are the tightest bounds known when the only information is the volume fraction of the particles-in other words, no other structural or statistical information is known.

7.2 Effective density of the material

The effective density of a mixture for a two-phase materials can directly be determined by

$$\begin{aligned}\rho^* &\stackrel{\text{def}}{=} \langle \rho(\boldsymbol{x}) \rangle_V \stackrel{\text{def}}{=} \frac{1}{V}\int_V \rho(\boldsymbol{x})\, dV \\ &= \frac{1}{V}\left(\int_{V_1} \rho_1\, dV + \int_{V_2} \rho_2\, dV\right) = v_1\rho_1 + v_2\rho_2.\end{aligned} \tag{28}$$

Furthermore

$$\begin{aligned}(\rho C)^* &\stackrel{\text{def}}{=} \langle \rho(\boldsymbol{x})C(\boldsymbol{x}) \rangle_V \stackrel{\text{def}}{=} \frac{1}{V}\int_V \rho(\boldsymbol{x})C(\boldsymbol{x})\, dV \\ &= \frac{1}{V}\left(\int_{V_1} \rho_1 C_1\, dV + \int_{V_2} \rho_2 C_2\, dV\right) \\ &= v_1\rho_1 C_1 + v_2\rho_2 C_2\end{aligned} \tag{29}$$

The density-oriented calculations are not estimates *they are exact*. The effective density of a mixture for a two-phase materials can directly be determined by

$$m = \rho^* V = (v_1\rho_1 + v_2\rho_2)\frac{4}{3}\pi R^3, \tag{30}$$

where $V = \frac{4}{3}\pi R^3$, while the effective thermal mass is

$$mC = (\rho C)^* V = (v_1\rho_1 C_1 + v_2\rho_2 C_2)\frac{4}{3}\pi R^3. \tag{31}$$

7.3 Effective charge-carrying capacity of the material

$$\begin{aligned}q^* &\stackrel{\text{def}}{=} \langle q(\boldsymbol{x}) \rangle_V \stackrel{\text{def}}{=} \frac{1}{V}\int_V q(\boldsymbol{x})\, dV = \frac{1}{V}\left(\int_{V_1} q_1\, dV + \int_{V_2} q_2\, dV\right) \\ &= v_1\langle q_1 \rangle_{V_1} + v_2\langle q_2 \rangle_{V_2}.\end{aligned} \tag{32}$$

Depending on the materials under consideration, either the carrier material and/or the particles could carry a charge.

Remark There exist a large number of effective property estimation techniques, and we refer the reader to Torquato [24], Jikov et al. [25], Hashin [23], Mura [26], Markov [27] for theoretical aspects and for more computationally-oriented approaches, Ghosh [28], Ghosh and Dimiduk [29], Matous et al [30] and Zohdi and Wriggers [31], Zohdi [32]. It is important to note that direct numerical approaches, discretizing the entire particle-laden heterogeneous domain with a very fine mesh, are quite accurate, but inordinately computationally expensive. If is for this reason that multiscale models are frequently used, which employ less computationally-intensive effective property models in most of the domain and detailed microstructural models in critical regions (see Zohdi and Wriggers [31] for reviews).

8 Integration of the equations

With the governing equations established, one can then integrate Eq. 10 to obtain the velocity for the ith lumped mass with a simple Forward–Euler integration[3]

$$\begin{aligned}\boldsymbol{v}_i(t+\Delta t) &= \boldsymbol{v}_i(t) + \frac{1}{m_i}\int_t^{t+\Delta t} \boldsymbol{\Psi}_i^{tot}(t)\, dt \approx \boldsymbol{v}_i(t) \\ &\quad + \frac{\Delta t}{m_i}\boldsymbol{\Psi}_i^{tot}(t),\end{aligned} \tag{33}$$

and the position for the ith lumped mass by applying the integration process again:

[3] More sophisticated implicit solution methods for strongly interacting multi-component systems can be found in Zohdi [33,33–44].

$$\boldsymbol{r}_i(t+\Delta t) \approx \boldsymbol{r}_i(t) + \Delta t\, \boldsymbol{v}_i(t), \tag{34}$$

which provides an updating scheme for the set equations for $i = 1, 2, 3, ..., N_d$ lumped masses. For the thermal states

$$\begin{aligned}\theta_i(t+\Delta t) &= \theta_i(t) + \frac{1}{m_i C_i}\left(\int_t^{t+\Delta t} \mathcal{Q}_i\, dt + \int_t^{t+\Delta t} \mathcal{H}_{ci}\, dt \right.\\ &\quad \left. + \int_t^{t+\Delta t} \mathcal{H}_{ri}\, dt + \int_t^{t+\Delta t} \mathcal{H}_{di}\, dt\right)\\ &\approx \theta_i(t) + \frac{\Delta t}{m_i C_i}\left(\mathcal{Q}_i(t) + \mathcal{H}_{ci}(t)\right.\\ &\quad \left. + \mathcal{H}_{ri}(t) + \mathcal{H}_{di}(t)\right). \end{aligned} \tag{35}$$

8.1 Overall solution algorithm

The algorithm is as follows:

(1) COMPUTE ROBOT SYSTEM POSITION TIME = t :

(2) SET i = 1 :

(3) IF i > N_d THEN GO TO (5)

(4) IF i ≤ N_d THEN : (FOR LUMPED MASS i)

- (*a*) COMPUTE POSITION : $\boldsymbol{r}_i(t+\Delta t)$
- (*b*) COMPUTE TEMPERATURE : $\theta_i(t+\Delta t)$
- (*c*) GO TO (3) AND NEXT DROP/LUMPED MASS ($i = i+1$)

(5)INCREMENT TIME : $t = t + \Delta t$

(36)

Table 1 Material parameters used in the example

Parameter	Value
Link one angular velocity	$\dot{\Theta}_1 = -10$ rad/s
Link two angular velocity	$\dot{\Theta}_2 = -1$ rad/s
Link three angular velocity	$\dot{\Theta}_3 = 10$ rad/s
Dispensing velocity	$\Delta v^{d-e} = 1$ m/s
Link one	$L_1 = 1$ m
Link two	$L_2 = 1$ m
Link three	$L_3 = 0.5$ m
Surrounding cooling fluid velocity	$\boldsymbol{v}_f = (10, 0, 0)$ m/s
Surrounding convective cooling coefficient	$h = 100$ W/(m^{2}K)
Volume fraction of phases 2	$v_1 = 0.75$ and $v_2 = 0.25$)
Phase 1 mass density	$\rho_1 = 2000$ kg/m^3
Phase 2 mass density	$\rho_2 = 7000$ kg/m^3
Temperature of the robot	400 K
Phase 1 heat capacity of the droplet	C = 1000 J/(kg K)
Phase 2 heat capacity of the droplet	C = 1000 J/(kg K)
Ambient temperature	$\theta_o = 325$ K
Droplet radius	$R = 0.001$ m
Phase 1 thermal conductivity	$\mathbb{K}_1 = 10$ W/(m K)
Phase 2 thermal conductivity	$\mathbb{K}_2 = 20$ W/(m K)
Pixel charge	$q_p = (1 \times 10^{-7}, 0)$ C
Pixel grid	10×10 pixels
Per unit volume charge for phase 1	$\hat{q}_1 = 0$ C/m^3
Per unit volume charge for phase 2	$\hat{q}_2 = 1000$ C/m^3
Radiative efficiency	$\epsilon = 0.75$

8.2 Numerical example: fault tolerance vs. no fault tolerance

Consider the three-link mechanism introduced at the beginning of this paper, with material dispensed from the printer. The system parameters are shown in Table 1. The material that exits the printer initially has the temperature and velocity of the print head. The angular velocities are constant in this simple example. Ten-thousand time steps were used. The wall-clock simulation time was on the order of 0.03 s on a Macbook-Pro using a FORTRAN-90 code written by the author. The results are shown in Figs. 4, 5 and 6, with and without the electrical charging. Clearly, with the charge, one can print within the target, despite the inaccuracy of the robot. The speed at which this type of simulation can be completed allows one to answer the inverse question of what the combination of parameters should be for a desired result. In order to cast the objective mathematically, we set the problem up as a Machine Learning Algorithm (MLA). Following Zohdi [46], we formulate the objective as a cost-function minimization problem whereby a pattern at time $t = T = 1$ s is given by (Fig. 7)

- Specifying the desired locations of the drops: $\boldsymbol{r}_i^{des}(t)$, $i = 1, ..., N_d$ at time $t = T$,
- Determining where the drops have been placed by a trial set of parameter: $\boldsymbol{r}_i^{gen}(t)$, $i = 1, ..., N_d$ at time $t = T$,
- Determining the difference the desired and generated patterns:

$$\Pi = \frac{\sum_{i=1}^{N_d} ||\boldsymbol{r}_i^{des} - \boldsymbol{r}_i^{gen}||}{\sum_{i=1}^{N_d} ||\boldsymbol{r}_i^{des}||}, \tag{37}$$

- Systematically minimize Equation 37, $min_{\Lambda}\, \Pi$, by varying the design parameters: $\boldsymbol{\Lambda}^i \stackrel{\text{def}}{=} \{\Lambda_1^i, \Lambda_2^i, \Lambda_3^i, \Lambda_4^i, ..., \Lambda_N^i\} \stackrel{\text{def}}{=} \{\dot{\Theta}_1, \dot{\Theta}_2, \dot{\Theta}_3, \Delta \boldsymbol{v}^e, q_p\}$.
- The system parameter search is conducted within the constrained ranges of $\dot{\Theta}_1^{(-)} \leq \dot{\Theta}_1 \leq \dot{\Theta}_1^{(+)}$, $\dot{\Theta}_2^{(-)} \leq \dot{\Theta}_2 \leq \dot{\Theta}_2^{(+)}$, $\dot{\Theta}_3^{(-)} \leq \dot{\Theta}_3 \leq \dot{\Theta}_3^{(+)}$, $\Delta \boldsymbol{v}^{e(-)} \leq \Delta \boldsymbol{v}^e \leq \Delta \boldsymbol{v}^{e(+)}$ and $q_p^{(-)} \leq q_p \leq q_p^{(+)}$. These upper and lower limits would, in general, be dictated by what is physically possible with the machinery and materials available.

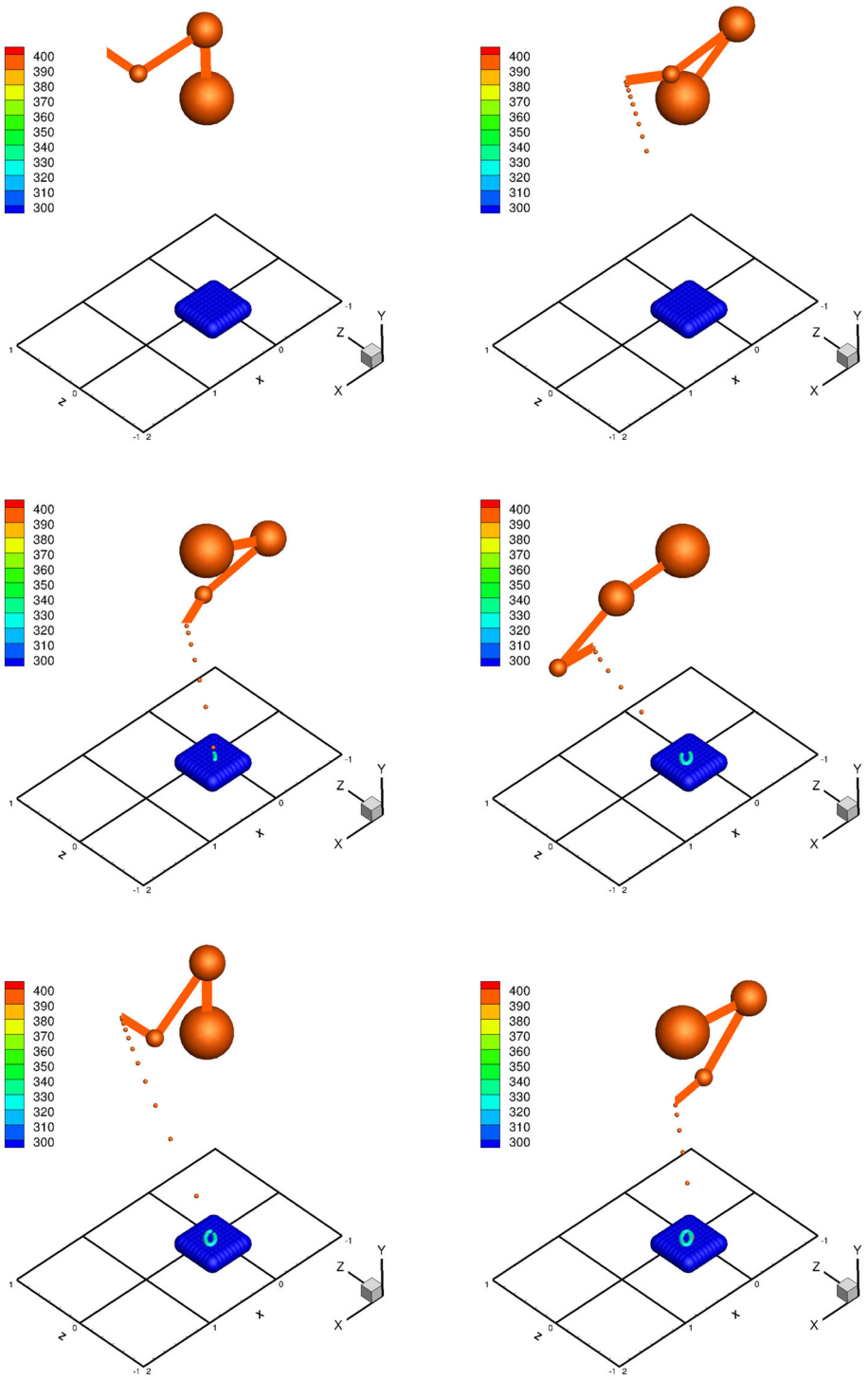

Fig. 4 With fault-tolerance charging—a deposition pattern: left to right and top to bottom. The colors indicate the temperature. The robot temperature was 400 K (color coded orange) while the substrate was set as 300 K (color coded dark blue). The total time was $T = 1$ s and the time slabs are $T = 0, 1/6, 1/3, 1/2, 2/3$ and 1 s. The robot started at position $\Theta_1 = \pi/2$, $\Theta_2 = 0$ and $\Theta_3 = 0$. (Color figure online)

8.3 System parameter search: Machine Learning Algorithm (MLA)

Here we follow Zohdi [45,46] in order to minimize Equation 37, which we will refer to as a "cost function". Cost functions such as Eq. 37 are nonconvex in design parameter space and often nonsmooth. Their minimization is usually difficult with direct application of gradient methods. This motivates nonderivative search methods, for example those found in Machine Learning Algorithms (MLA's). One of the most basic subset of MLA's are so-called Genetic Algorithms (GA's). Typically, one will use a GA first in order

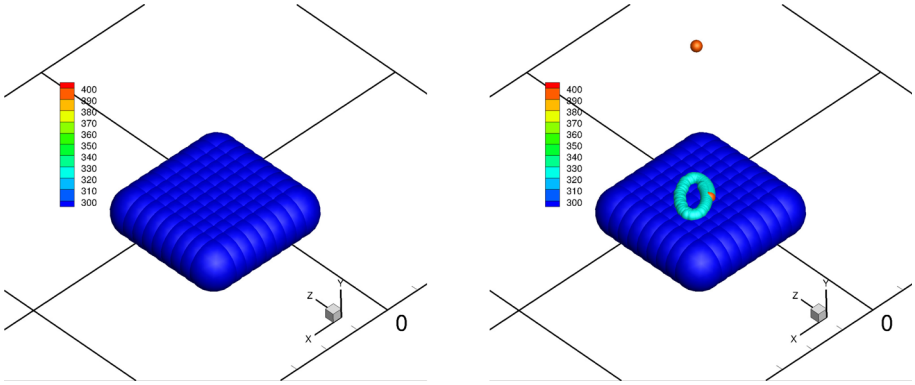

Fig. 5 A zoom on the drops being deposited on the electrified pattern in Fig. 4

to isolate multiple local minima, and then use a gradient based algorithm in these locally convex regions or reset the GA to concentrate its search over these more constrained regions. GA's are typically the simplest schemeto start the analysis, and one can, of course, use more sophisticated methods if warranted. For a review of GA's, see the pioneering work of Holland ([47]), as well as Goldberg [48], Davis [49], Onwubiko [50], Lagaros et al. [51], Papadrakakis et al. [52–55] and Goldberg and Deb [56]. The GA approach is extremely well-suited for nonconvex, nonsmooth, multicomponent, multistage systems, and involves the following essential concepts:

1. *Population generation* Generate system population: $\mathbf{\Lambda}^i \stackrel{\text{def}}{=} \{\Lambda_1^i, \Lambda_2^i, \Lambda_3^i, \Lambda_4^i, ..., \Lambda_N^i\} = \{\dot{\Theta}_1, \dot{\Theta}_2, \dot{\Theta}_3, \Delta \boldsymbol{v}^e, q_p\}^i$
2. *Performance evaluation* Compute fitness/performance of each genetic string: $\Pi(\mathbf{\Lambda}^i)$ and rank them $(i = 1, ..., N)$
3. *Mating process* Mate pairs/produce offspring: $\boldsymbol{\lambda}^i \stackrel{\text{def}}{=} \Phi^{(I)}\mathbf{\Lambda}^i + (1 - \Phi^{(I)})\mathbf{\Lambda}^{i+1}$ where $0 \leq \Phi \leq 1$ (Fig. 8
4. *Gene elimination* Eliminate poorly performing genetic strings, keep top parents and generated offspring
5. *Population regeneration* Repeat the process with the new gene pool and new *random* genetic strings
6. *Solution post-processing* Employ gradient-based methods afterwards in the local "valleys"-*if smooth enough*

8.3.1 Algorithmic specifics

Following Zohdi [45,46], the algorithm is as follows:

- *Step 1* Randomly generate a population of S starting genetic strings, $\mathbf{\Lambda}^i, (i = 1, 2, 3, ..., S) : \mathbf{\Lambda}^i \stackrel{\text{def}}{=} \{\Lambda_1^i, \Lambda_2^i, \Lambda_3^i, \Lambda_4^i, ..., \Lambda_N^i\} \stackrel{\text{def}}{=} \{\dot{\Theta}_1, \dot{\Theta}_2, \dot{\Theta}_3, \Delta \boldsymbol{v}^e, q_p\}$
- *Step 2* Compute fitness of each string $\Pi(\mathbf{\Lambda}^i)$, (i=1, ..., S)
- *Step 3* Rank genetic strings: $\mathbf{\Lambda}^i$, (i=1, ..., S)
- *Step 4* Mate nearest pairs and produce two offspring, (i=1, ..., S) $\boldsymbol{\lambda}^i \stackrel{\text{def}}{=} \Phi^{(I)}\mathbf{\Lambda}^i + (1 - \Phi^{(I)})\mathbf{\Lambda}^{i+1}$, $\boldsymbol{\lambda}^{i+1} \stackrel{\text{def}}{=} \Phi^{(II)}\mathbf{\Lambda}^i + (1 - \Phi^{(II)})\mathbf{\Lambda}^{i+1}$
- *Step 5* Eliminate the bottom $M < S$ strings and keep top $K < N$ parents and top K offspring (K offspring+K parents+M=S)
- *Step 6* Repeat STEPS 1-6 with top gene pool (K offspring and K parents), plus M new, randomly generated, strings
- *Note* $\Phi^{(I)}$ and $\Phi^{(II)}$ are random numbers, such that $0 \leq \Phi^{(I)} \leq 1$, $0 \leq \Phi^{(II)} \leq 1$, which are different for each component of each genetic string
- *Option* Rescale and restart search around best performing parameter set every few generations

Remark 1 If one selects the mating parameter Φ to be greater that one and/or less than zero, one can induce "mutations". i.e. characteristics that neither parent possesses. However, this is somewhat redundant with introduction of new random members of the population in the current algorithm.

Remark 2 If one does not retain the parents in the algorithm above, in is possible that inferior performing offspring may replace superior parents. Thus, top parents should be kept for the next generation. This guarantees a monotone reduction in the cost function. Furthermore, retained parents do not need to be re-evaluated-making the algorithm less computationally less expensive, since these parameter sets do not have to be reevaluated (or ranked) in the next generation. Numerous studies of the author have shown that advantages parent retention outweighs inbreeding, for sufficiently large population sizes. Finally, we remark that this algorithm is easily parallelizable.

8.4 MLA electrodynamic example

As a model problem, we used the result of the previous numerical example that generated the results and pattern in Fig. 4 using

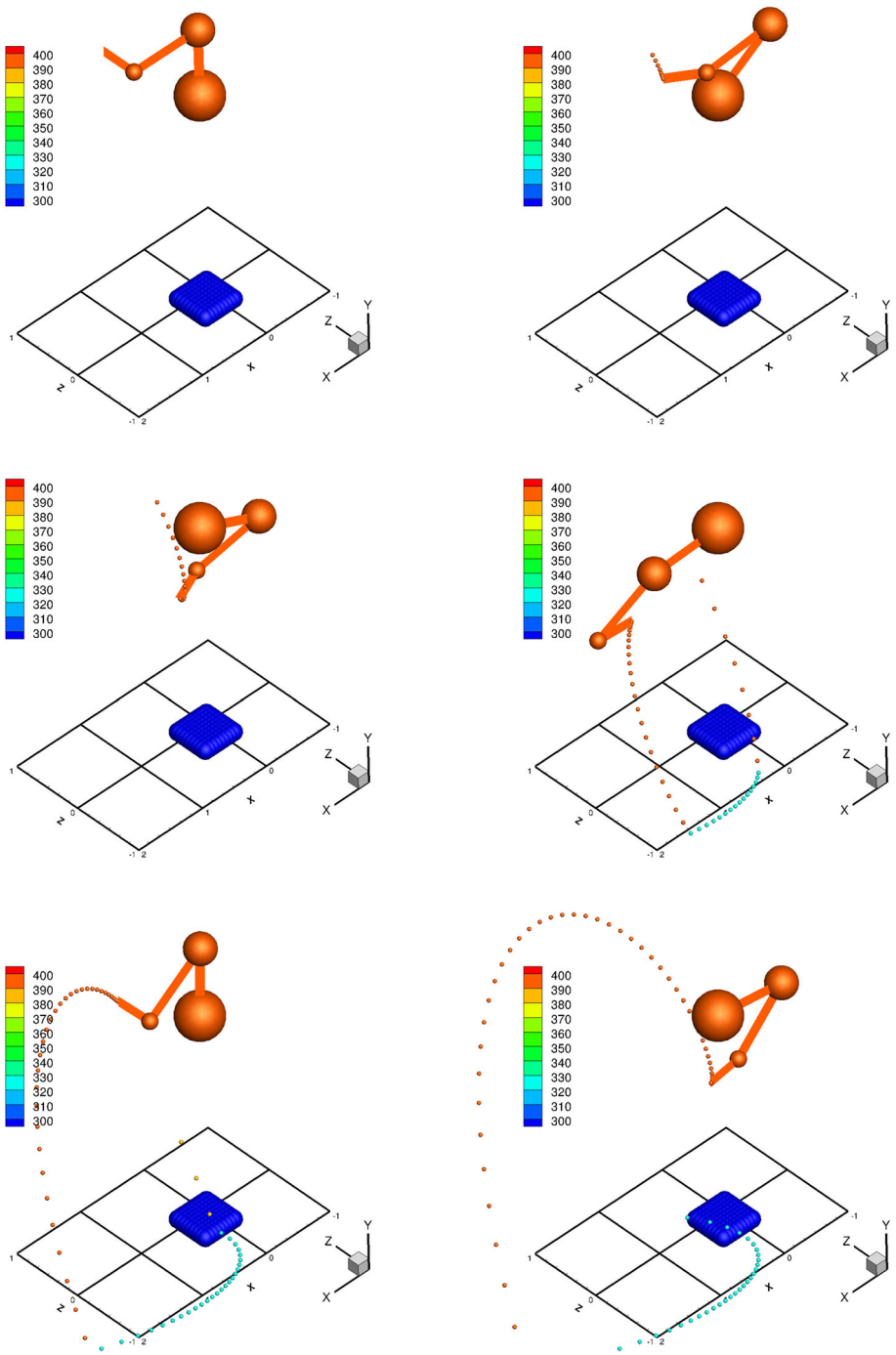

Fig. 6 Without fault-tolerance charging: a deposition pattern: left to right and top to bottom. The colors indicate the temperature. The robot temperature was 400 K (color coded orange) while the substrate was set as 300 K (color coded dark blue). The total time was $T = 1$ s and the time slabs are $T = 0, 1/6, 1/3, 1/2, 2/3$ and 1 s. The robot started at position $\Theta_1 = \pi/2$, $\Theta_2 = 0$ and $\Theta_3 = 0$. (Color figure online)

- $\dot{\Theta}_1 = -10$ rad/s,
- $\dot{\Theta}_2 = -1$ rad/s,
- $\dot{\Theta}_3 = 10$ rad/s,
- $\Delta v^d = 1$ m/s and
- $q_p = 10^{-7}$ C.

We used the following MLA settings:

- Number of design variables: 5,
- Search domain for $\dot{\Theta}_1$: $\dot{\Theta}_1^- = -5 \leq \dot{\Theta}_1 \leq -30 = \dot{\Theta}_1^+$,
- Search domain for $\dot{\Theta}_2$: $\dot{\Theta}_2^- = -0.5 \leq \dot{\Theta}_2 \leq -3 = \dot{\Theta}_2^+$,
- Search domain for $\dot{\Theta}_3$: $\dot{\Theta}_3^- = 5 \leq \dot{\Theta}_3 \leq 30 = \dot{\Theta}_3^+$,
- Search domain for Δv^d: $\Delta v^{e,-} = 0.5 \leq \Delta v^d \leq 3.5 = \Delta v^{e,+}$,
- Search domain for q_p: $q_p^- = 0 \leq q_p \leq 3 \times 10^{-7} = q_p^+$,
- Population size per generation: 20,
- Number of parents to keep in each generation: 4,
- Number of children created in each generation: 4,

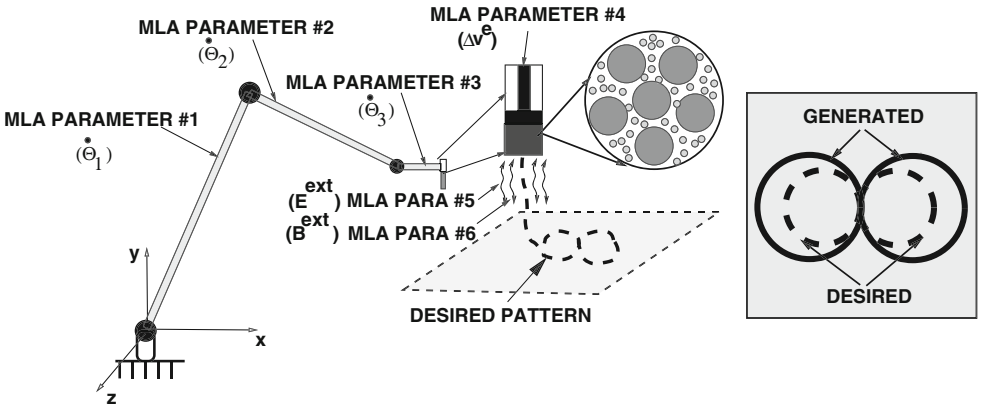

Fig. 7 Machine Learning Algorithm model problem of a robot with a dispensing printer head

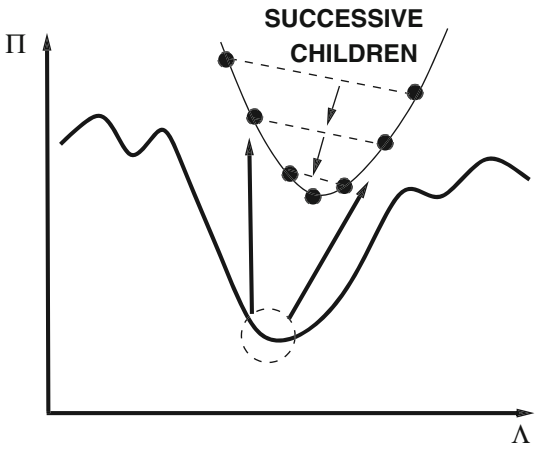

Fig. 8 The basic action of a genetic algorithm

- Number of completely new genes created in each generation: 12 and
- Number of generations: 200.

The algorithm was automatically reset every *30 generations*. The entire 200 generation simulation, with 20 genes per evaluation (8000 total designs) took on the order of 5 minutes of a laptop, *making it ideal as a design tool.* Figure 9 (average top four genes performance and top gene performance) and Table 2 (values of the gene components) illustrate the results. The MLA/GA is able to home in of a variety of possible designs, including the one corresponding to the original set of parameters that generated the test pattern and alternatives that achieve virtually the same results. This allows system designers to more flexibility in parameter selection. We note that, for a given set of parameters, a complete simulation takes on the order of 0.03 s, thus over 100,000 parameter sets can be evaluated in an hour, *without even exploiting the inherent parallelism of the MLA*. For more detailed micromechanical information on the behavior of the optimal result, Discrete Element Methods (DEM) are needed, and are discussed in the summary of this paper.

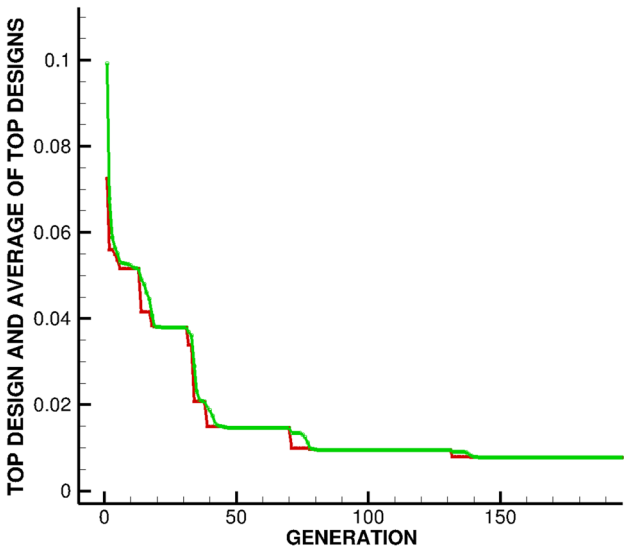

Fig. 9 Left-using the objective function (Π). Machine learning output, generation after generation. Shown are the best performing gene (design parameter set, in red) as a function of successive generations, as well as the average performance of the population of the top four genes (designs, in green). (Color figure online)

8.5 Extensions

In addition to the obvious use for industrial additive manufacturing processes, application of the methodology to the 3D bioprinting of flowing media containing cells is quite relevant. Over the last decade, there has been a steady increase in so-called bioprinting technology, whereby cells are combined with fluids containing nutrients, growth factors, etc, to make what is called a bioink. The slurry of material is then loaded into a 3D bioprinter that deposits the mixture, layer by layer onto a surface to build tissue-like structures, ligaments, cartilage, organs, for example on scaffolds or to make scaffolds. The liquid that the cells are immersed into provide the nutrients for the cells to remain alive. In some cases, the cells are encapsulated in a spherical shell within the fluid in order to keep the cells healthy. The field is rela-

Table 2 The top 10 system parameter performers

Design	$\dot{\Theta}_1$	$\dot{\Theta}_2$	$\dot{\Theta}_3$	Δv^e	q_p	Π
1	−5.94	−0.79	12.20	1.13	0.0000001285	0.0077391595
2	−8.48	−0.62	12.23	1.59	0.0000001169	0.0077464996
3	−9.13	−0.61	12.62	1.28	0.0000001214	0.0077469398
4	−7.91	−0.77	8.47	1.57	0.0000001237	0.0077470045
5	−9.06	−0.54	8.12	1.36	0.0000001122	0.0371113337
6	−8.47	−0.75	7.97	1.53	0.0000001310	0.0403717650
7	−8.50	−0.81	7.78	1.27	0.0000001207	0.0414568277
8	−9.00	−0.55	10.80	1.46	0.0000001462	0.0455584033
9	−8.37	−0.75	7.82	1.24	0.0000001463	0.0462887025
10	−8.74	−0.68	10.53	1.28	0.0000001227	0.0560576224

tively wide now (see [57–67]), but still has a common theme: the attempted deposition of a particle-embedded slurry. Some emerging variants of this technology have attempted to utilize electromagnetic fields. For example, magnetic 3D bioprinting attaches biocompatible magnetic nanoparticles to cells in order to magnetize them. Thereafter, the cells can be precisely and rapidly deposited onto patterns following the electromagnetic fields (see [68–76]). In this case, only a magnetic field is needed, since the cells are rendered magnetically sensitive due to added surfactants. We note that intrinsic magnetic (non-electromagnetic) forces can be approximated by a simple model, $\boldsymbol{\Psi}^{mag} = \nabla(\boldsymbol{m} \cdot \boldsymbol{B}^{ext}) = \nabla(\gamma \boldsymbol{B}^{ext} \cdot \boldsymbol{B}^{ext})$ (independently of the Lorentz forces), where γ is a material parameter that is related to the magnetization ($\boldsymbol{m}$; magnetic dipole properties, susceptibility, permeability, moment density, etc.) of the element (see Feynman et al. [77], Cullity and Graham [78], Boyer [79] or Jackson [17]). Thus, for a spatially varying magnetic field we have

$$\begin{aligned} \boldsymbol{\Psi}^{mag} &= \nabla(\gamma \boldsymbol{B}^{ext} \cdot \boldsymbol{B}^{ext}) = \gamma \nabla(\boldsymbol{B}^{ext} \cdot \boldsymbol{B}^{ext}) \\ &= 2\gamma(\nabla \boldsymbol{B}^{ext}) \cdot \boldsymbol{B}^{ext}, \end{aligned} \tag{38}$$

or explicitly

$$\boldsymbol{\Psi}^{mag} = 2\gamma(\nabla \boldsymbol{B}^{ext}) \cdot \boldsymbol{B}^{ext} = 2\gamma \begin{bmatrix} \frac{\partial B_1}{\partial x_1} & \frac{\partial B_1}{\partial x_2} & \frac{\partial B_1}{\partial x_3} \\ \frac{\partial B_2}{\partial x_1} & \frac{\partial B_2}{\partial x_2} & \frac{\partial B_2}{\partial x_3} \\ \frac{\partial B_3}{\partial x_1} & \frac{\partial B_3}{\partial x_2} & \frac{\partial B_3}{\partial x_3} \end{bmatrix}^{ext} \begin{Bmatrix} B_1 \\ B_2 \\ B_3 \end{Bmatrix}^{ext}, \tag{39}$$

In this case, we could construct the following additional genetic string

$$\boldsymbol{\Lambda}^{mag} = \left\{ \frac{\partial B_1}{\partial x_1}, \frac{\partial B_1}{\partial x_2}, \frac{\partial B_1}{\partial x_3}, \frac{\partial B_2}{\partial x_1}, \frac{\partial B_2}{\partial x_2}, \frac{\partial B_2}{\partial x_3}, \frac{\partial B_3}{\partial x_1}, \frac{\partial B_3}{\partial x_2}, \frac{\partial B_3}{\partial x_3} \right\}, \tag{40}$$

which would generalize the one used previously to read

$$\boldsymbol{\Lambda} = \{\dot{\Theta}_1, \dot{\Theta}_2, \dot{\Theta}_3, \Delta \boldsymbol{v}^d, \boldsymbol{E}^{ext}, \boldsymbol{B}^{ext}, \nabla \boldsymbol{B}^{ext}\}, \tag{41}$$

explicitly,

$$\begin{aligned} \boldsymbol{\Lambda} = \Big\{ &\dot{\Theta}_1, \dot{\Theta}_2, \dot{\Theta}_3, \Delta \boldsymbol{v}^d, E_1^{ext}, E_2^{ext}, E_3^{ext}, B_1^{ext}, B_2^{ext}, B_3^{ext}, \\ &\frac{\partial B_1}{\partial x_1}, \frac{\partial B_1}{\partial x_2}, \frac{\partial B_1}{\partial x_3}, \frac{\partial B_2}{\partial x_1}, \frac{\partial B_2}{\partial x_2}, \frac{\partial B_2}{\partial x_3}, \frac{\partial B_3}{\partial x_1}, \frac{\partial B_3}{\partial x_2}, \frac{\partial B_3}{\partial x_3} \Big\}. \end{aligned} \tag{42}$$

9 Summary and extensions

As outlined in this paper, free-form printing of particle-functionalized materials consist of attaching a dispenser to a robot arm, which then releases the mixture in free-space. These approaches are becoming popular because they utilize widely-available highly-programmable robots. However, often the release of a complex mixture in free-space is somewhat imprecise, thus electrical field control has been proposed as one possible remedy to enhance the precision of such processes. Specifically, enhanced control of the material is achieved by electrifying the released material in the presence of a prescribed ambient electrical field, in order to guide it to the desired position. There are many components that comprise such a system, thus motivating the construction of a simulation tool framework assembling submodels of (1) The kinematics of the robot arm and the dispenser-printer head, (2) The electrical and gravitational forces on the released material, (3) The dynamics of the released material and (4) The conductive, convective and radiative cooling of the media. The modular system structure allows for easy replacement of submodels within the overall framework. Afterwards, a Machine Learning Algorithm (MLA) was developed to identify and optimize the proper system parameters which deliver a desired printed pattern. Had the particle noninteraction approximation not been invoked, a coupled system of equations would arise due to the interaction between the constituents that comprise the released material. This leads to a coupled set of equations. In order to illustrate how such material system are modeled, following Zohdi [15,33–44], we consider a collection of N_p non-intersecting particles (which comprise the

microconstituents in the material in the droplets), which are assumed to be spherical in shape. It is also assumed that the particles are small enough that their rotation with respect to their mass center minimally affects their overall motion (this is discussed further shortly). For an arbitrary ith particle in the system, acted upon by (Zohdi [15,33–44])

1. $\boldsymbol{\Psi}_i^{con}$: inter-particle contact forces,
2. $\boldsymbol{\Psi}_i^{bond}$: inter-particle adhesive bonding forces,
3. $\boldsymbol{\Psi}_i^{ext}$: inter-particle near-field and external forces and
4. $\boldsymbol{\Psi}_i^{drag}$: particle drag forces from any surrounding gas,

the dynamics are governed by

$$m_i \ddot{\boldsymbol{r}}_i = \boldsymbol{\Psi}_i^{con} + \boldsymbol{\Psi}_i^{bond} + \boldsymbol{\Psi}_i^{ext} + \boldsymbol{\Psi}_i^{drag} \stackrel{\text{def}}{=} \boldsymbol{\Psi}_i^{tot}(\boldsymbol{r}_1, \boldsymbol{r}_2, ..., \boldsymbol{r}_{N_p}), \tag{43}$$

where $\boldsymbol{r}_i$ is the position vector of the ith particle and $\boldsymbol{\Psi}_i^{tot}$ is the total of the forces acting on the ith particle with analogous equations for the heat-transfer. For example, the heat transfer of each particle $i = 1, 2, ..., N_p$, $m_i C_i \dot{\theta}_i = \mathcal{Q}_i + \mathcal{H}_i$, where $\mathcal{Q}_i$ represents the conductive contribution from surrounding particles in contact (including the substrate), and $\mathcal{H}_i$ represents the external heating terms. Complex, coupled, particle systems such as the above can be efficiently solved in a staggered manner by (at a given time increment): (1) solving each field equation individually, "freezing" the other (coupled) fields in the system, allowing only the primary field to be active and (2) updating the primary field variable after the solution of each field equation. The next field equation is treated in a similar manner where, as the physics changes, the field that is most sensitive (exhibits the largest amount of relative nondimensional change) dictates the time-step size. This is an implicit, staggered, adaptive time-stepping scheme. Such approaches have a long history in the computational mechanics community (see, for example, Zienkiewicz [80], Zienkiewicz et al. [81], Lewis et al. [82], Lewis and Schrefler [83], Park and Felippa [84], Farhat at al [85], Farhat and Lesoinne [86], Farhat et al. [87], Piperno [88], Piperno et al. [89], Piperno and Farhat [90] and Michopoulos et al. [91], Lesoinne and Farhat [92] and Le Tallec and Muoro [93]. In Zohdi [15,33–44] this process proceeds by first solving for the particle positions, assuming the thermal fields fixed (cast in an abstract operator setting for clarity):

$$\mathcal{A}_1(\underline{\boldsymbol{r}^{L+1,K}}, \theta^{L+1,K-1}) = \mathcal{F}_1(\boldsymbol{r}^{L+1,K-1}, \theta^{L+1,K-1}), \tag{44}$$

and then solving for the thermal fields, assuming the particle positions fixed:

$$\mathcal{A}_2(\boldsymbol{r}^{L+1,K}, \underline{\theta^{L+1,K}}) = \mathcal{F}_2(\boldsymbol{r}^{L+1,K}, \theta^{L+1,K-1}), \tag{45}$$

where only the underlined variable is "active", L indicates the time step and K indicates the iteration counter. Within the staggering scheme, implicit time-stepping methods, with time step size adaptivity can be used, which are dictated by controlling the normalized errors within each time step for the dynamical and thermodynamic fields,

$$\varpi_{rK} \stackrel{\text{def}}{=} \frac{||\boldsymbol{r}^{L+1,K} - \boldsymbol{r}^{L+1,K-1}||}{||\boldsymbol{r}^{L+1,K} - \boldsymbol{r}^{L}||} \quad \text{and}$$
$$\varpi_{\theta K} \stackrel{\text{def}}{=} \frac{||\theta^{L+1,K} - \theta^{L+1,K-1}||}{||\theta^{L+1,K} - \theta^{L}||}. \tag{46}$$

Details are provided in the Zohdi [15,33–44]. However, the essentials are that an"overlap" (contact) model is used to determine the normal contact forces between particles, where for the ith particle in contact with N_{ci} particles, a total contact force of $\boldsymbol{\Psi}_i^{con,n} = \sum_{j=1}^{N_{ci}} \boldsymbol{\psi}_{ij}^{con,n}$ is produced, where the forces are dictated by the separation distance between the particle centers for the particle in contact, written generally as $\boldsymbol{\Psi}_{ij}^{con,n} = \mathcal{F}(||\boldsymbol{r}_i - \boldsymbol{r}_j||, R_i, R_j, material\ properties)$, R_i and R_j being the radii of the ith and jth particles in contact. Although including particle rotations is questionable for extremely small powders (idealized as spherical particles), for completeness, Zohdi [15] illustrated the inclusion of rotational equations of motion (a balance of angular momentum), which augment a balance of linear momentum, $m_i \dot{\boldsymbol{v}}_i = \boldsymbol{\Psi}_i^{tot}$, $\boldsymbol{v}_i$ being the center of mass velocity. The balance of angular momentum reads as $\dot{\boldsymbol{H}}_{i,cm} = \frac{d(\overline{I}_i \cdot \boldsymbol{\omega}_i)}{dt} = \boldsymbol{M}_{i,cm}^{tot}$, where, for spheres, we have $\boldsymbol{H}_{i,cm} = \overline{I}_{i,s}\boldsymbol{\omega}_i = \frac{2}{5} m_i R_i^2 \boldsymbol{\omega}_i$, where the total moment, $\boldsymbol{M}_{i,cm}^{tot}$, is due to interaction forces, contact forces and rolling resistance. Additionally, in such simulations, the electromagnetic forces are decomposed into three parts: (1) Lorentz forces (for charged particles), (2) *inter-particle near-field forces* and (3) magnetic forces (for magnetic particles). There exist a large number of empirical near-field relations that generally fall under the subject matter of the large field of Molecular Dynamics (MD), and we refer readers to Frenklach and Carmer [94], Haile [95], Hase [96], Schlick [19] and Rapaport [97], where Lennard–Jones, Mie and Morse potentials (Moelwyn-Hughes [99]) are usually employed, with various extensions such as Tersoff [100] additions and three-body terms (Stillinger [101]).

An example of the level of detail that one can extract from such a process is given in Figs. 10 and 11, using parameters found in Zohdi [15]. The initial stream of particles breaks into two aggregate drops. The aggregate drop that is closer to the electrified target (with electric field given by Equation 13) becomes attracted first, followed by the second drop that connects and recombines with the other to form a final deposition upon the target, which would eventually cool down. In such simulations, implementation of particle inter-

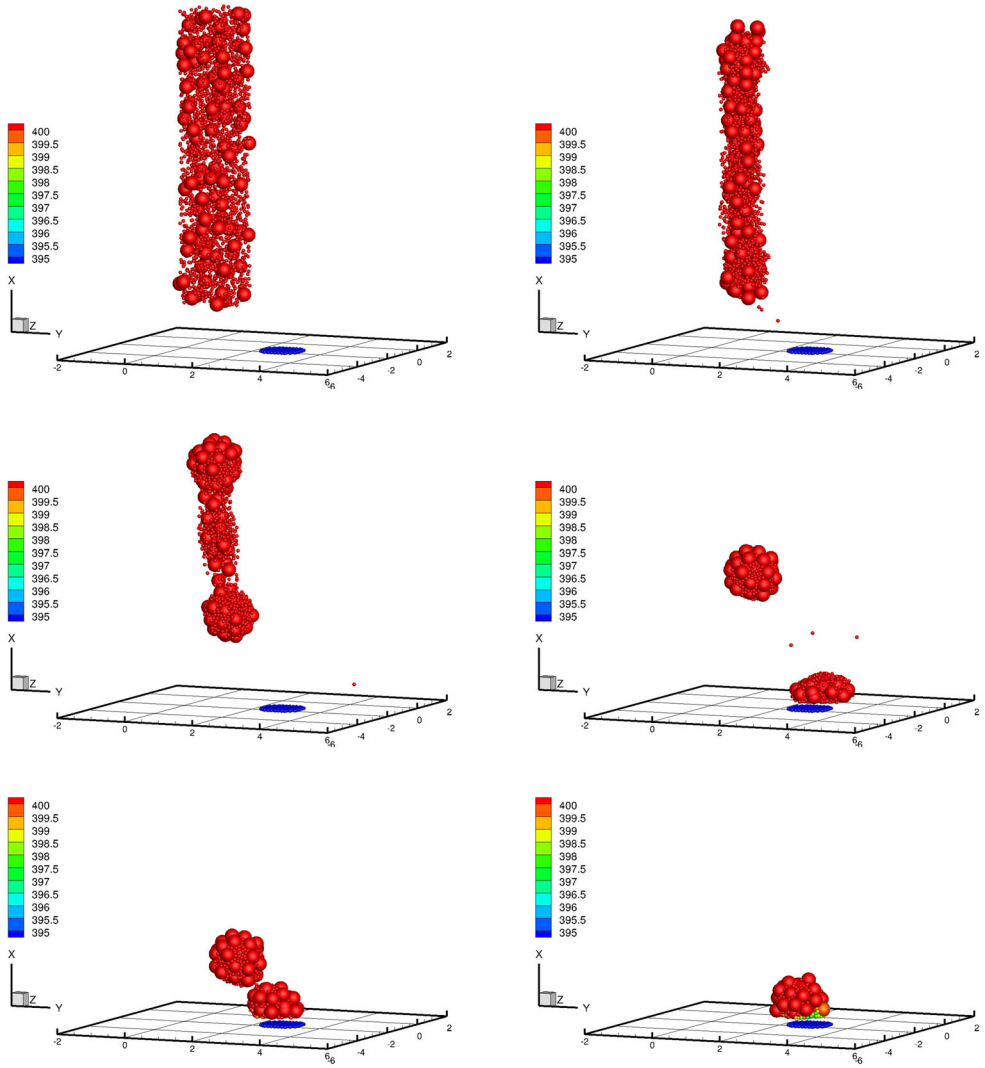

Fig. 10 A sequence of frames of the dynamics of stream of charged particles initially released from a dispenser near an electrified target is shown. The colors indicate the temperature of the materials (red = 400 K and dark blue = 300 K). The initial stream of particles breaks into two aggregate drops. The aggregate drop that is closer to the charged target becomes attracted first, followed by the second drop that connects and melds with the other to form a final deposition onto the target. (Color figure online)

action lists are key to speed-up calculations. This allows for efficient extension to very large particle systems. For each particle, these approaches proceed by determining neighboring particles within a radius of influence, and using only those particles for the particle in question. The list is then updated periodically during the simulations, and dramatically reduces the contact search computation ($\mathcal{O}(N_p^2)$ complexity, where N_p are the number of particles in the system), as well as other intra-particle operations. In the simulation results presented in Figs. 10 and 11, a nearest-neighbor list was constructed at the beginning of the simulation and for a subinterval of time, the interaction for each particle was restricted to these neighbors. Thereafter, the lists were updated after that interval expired and the process was repeated. We refer the reader to Zohdi [40–44] and Zohdi [15] for details. The use of such methods with the introduced MLA is under current investigation by the author.

However, one issue is that higher fidelity models are computationally more expensive, relative to the model used in the first part of this paper. Thus, in may be advantageous to utilize Neural Network-type paradigms which are based on constructing simple input-output type models that are, essentially, adaptive nonlinear regressions of the form $OUTPUT = \mathcal{B}(INPUT, W_1, W_2, ...W_N)$ where $\mathcal{B}$ is an Artificial Neural Network (ANN, Fig. 12) constructed from:

- *Synapses*, which multiply inputs by weights that represent the inputs' relevance to the desired output,

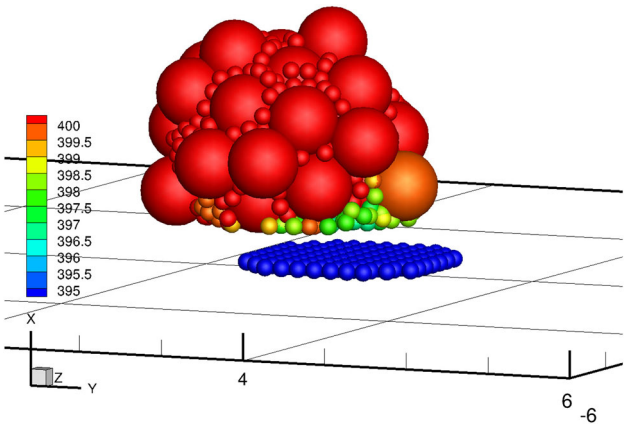

Fig. 11 A zoom on the material deposition onto an electrified target is shown. As indicated before, the initial stream of particles breaks into two aggregate drops. The aggregate drop that is closer to the charged target becomes attracted first, followed by the second drop that connects and melds with the other to form a final deposition onto the target

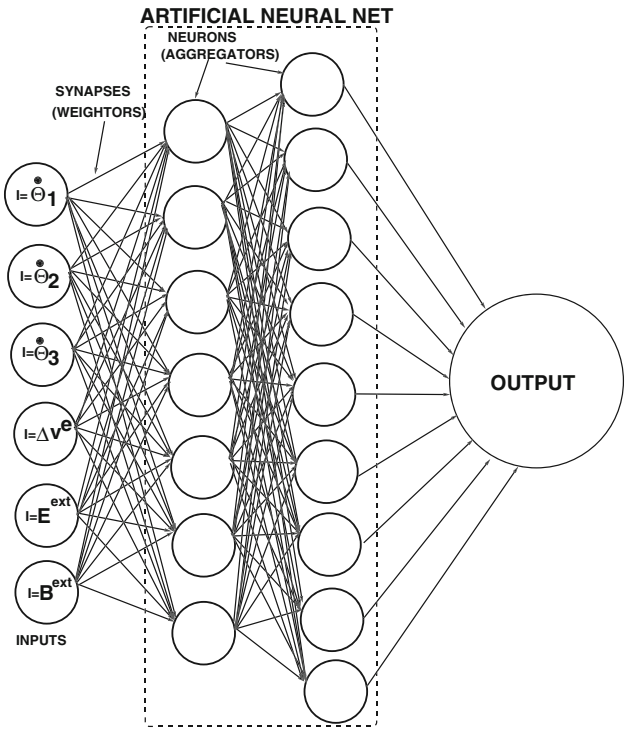

Fig. 12 A schematic of a neural net for the system considered in this paper

- *Neurons*, which add outputs from all incoming synapses and applies activation functions and
- *Training*, which recalibrates the weights to achieve a desired overall output.

Ultimately, one constructs a system with optimized weights to mimic an artificial "input-output" brain. For physically-complex systems, these techniques remain unproven, but are actively being investigated in a number of scientific fields. Their *robust* usefulness in the domain of multistage additive manufacturing processes is an open question that is under current investigation by the author.

References

1. Zohdi TI, Dornfeld DA (2015) Future synergy between computational mechanics and advanced additive manufacturing. US National Academies Report. http://sites.nationalacademies.org/cs/groups/pgasite/documents/webpage/pga_166813.pdf
2. Huang Y, Leu MC, Mazumdar J, Donmez A (2015) Additive manufacturing: current state, future potential, gaps and needs, and recommendation. J Manuf Sci Eng 137:014001–1
3. Hunt KH (1979) Kinematic geometry of mechanisms. Oxford engineering science series. Oxford University Press, Oxford
4. Hartenberg RS, Denavit J (1964) Kinematic synthesis of linkages. McGraw-Hill, New York
5. Howell LL (2001) Compliant mechanisms. Wiley, Hoboken
6. McCarthy JM, Soh GS (2010) Geometric design of linkages. Springer, New York
7. McCarthy JM (1990) Introduction to theoretical kinematics. MIT Press, Cambridge
8. Reuleaux F (1876) The kinematics of machinery (trans. and annotated by A. B. W. Kennedy) reprinted by Dover, New York (1963)
9. Sandor GN, Erdman AG (1984) Advanced mechanism design: analysis and synthesis, vol 2. Prentice-Hall, Englewood Cliffs
10. Slocum A (1992) Precision machine design. SME, Southfield
11. Suh CH, Radcliffe CW (1978) Kinematics and mechanism design. Wiley, New York
12. Uicker JJ, Pennock GR, Shigley JE (2003) Theory of machines and mechanisms. Oxford University Press, New York
13. Papageorgiou DT (1995) On the breakup of viscous liquid threads. Phys Fluids 7(7):15291521
14. Eggers J (1997) Nonlinear dynamics and breakup of free-surface flows. Rev Mod Phys 69(3):865
15. Zohdi TI (2017) Laser-induced heating of dynamic depositions in additive manufacturing. Methods Appl Mech Eng Comput. https://doi.org/10.1016/j.cma.2017.11.003
16. Zohdi TI (2017) On simple scaling laws for pumping fluids with electrically-charged particles. Int J Eng Sci. https://doi.org/10.1016/j.ijengsci.2017.11.003
17. Jackson JD (1998) Classical electrodynamics, 3rd edn. Wiley, New York
18. Chow CY (1980) An introduction to computational fluid dynamics. Wiley, New York
19. Schlichtling H (1979) Boundary-layer theory, 7th edn. McGraw-Hill, New York
20. Whitaker S (1972) Forced convection heat transfer correlations for flow in pipes, past flat plates, single cylinders, single spheres, and flow in packed beds and tube bundles. AIChE J 18:361371
21. Hashin Z, Shtrikman S (1962) On some variational principles in anisotropic and nonhomogeneous elasticity. J Mech Phys Solids 10:335–342
22. Hashin Z, Shtrikman S (1963) A variational approach to the theory of the elastic behaviour of multiphase materials. J Mech Phys Solids 11:127–140
23. Hashin Z (1983) Analysis of composite materials: a survey. ASME J Appl Mech 50:481–505
24. Torquato S (2002) Random heterogeneous materials: microstructure and macroscopic properties. Springer, New York
25. Jikov VV, Kozlov SM, Olenik OA (1994) Homogenization of differential operators and integral functionals. Springer, New York

26. Mura T (1993) Micromechanics of defects in solids, 2nd edn. Kluwer Academic Publishers, Alphen aan den Rijn
27. Markov KZ (2000) Elementary micromechanics of heterogeneous media. In: Markov Z, Preziozi L (eds) Heterogeneous media micromechanics modeling methods and simulations k. Birkhauser, Boston, pp 1–162
28. Ghosh S (2011) Micromechanical analysis and multi-scale modeling using the voronoi cell finite element method. CRC Press/Taylor & Francis, Boca Raton
29. Ghosh S, Dimiduk D (2011) Computational methods for microstructure–property relations. Springer, New York
30. Matouša K, Geers MGD, Kouznetsova VG, Gillman A (2017) A review of predictive nonlinear theories for multiscale modeling of heterogeneous materials. J Comput Phys 330:192–220
31. Zohdi TI, Wriggers P (2005, 2008) Introduction to computational micromechanics. Second Reprinting (*PeerReviewed*). Springer, New York
32. Zohdi TI (2012) Electromagnetic properties of multiphase dielectrics. A primer on modeling, theory and computation. Springer, New York
33. Zohdi TI (2002) An adaptive-recursive staggering strategy for simulating multifield coupled processes in microheterogeneous solids. Int J Numer Methods Eng 53:1511–1532
34. Zohdi TI (2004) Modeling and simulation of a class of coupled thermo-chemo-mechanical processes in multiphase solids. Comput Methods Appl Mech Eng 193(6–8):679–699
35. Zohdi TI (2004) Modeling and direct simulation of near-field granular flows. Int J Solids Struct 42(2):539–564
36. Zohdi TI (2005) Charge-induced clustering in multifield particulate flow. Int J Numer Methods Eng 62(7):870–898
37. Zohdi TI (2007) Computation of strongly coupled multifield interaction in particle–fluid systems. Comput Methods Appl Mech Eng 196:3927–3950
38. Zohdi TI (2010) On the dynamics of charged electromagnetic particulate jets. Arch Comput Methods Eng 17(2):109–135
39. Zohdi TI (2010) Simulation of coupled microscale multiphysical-fields in particulate-doped dielectrics with staggered adaptive FDTD. Comput Methods Appl Mech Eng 199:79–101
40. Zohdi TI (2013) Numerical simulation of charged particulate cluster-droplet impact on electrified surfaces. J Comput Phys 233:509–526
41. Zohdi TI (2014) Additive particle deposition and selective laser processing—a computational manufacturing framework. Comput Mech 54:171–191
42. Zohdi TI (2014) Embedded electromagnetically sensitive particle motion in functionalized fluids. Comput Part Mech 1:27–45
43. Zohdi TI (2015) Modeling and simulation of cooling-induced residual stresses in heated particulate mixture depositions. Comput Mech 56:613–630
44. Zohdi TI (2015) Modeling and efficient simulation of the deposition of particulate flows onto compliant substrates. Int J Eng Sci 99:74–91. https://doi.org/10.1016/j.ijengsci.2015.10.012
45. Zohdi TI (2003) Genetic design of solids possessing a random-particulate microstructure. Philos Trans R Soc Math Phys Eng Sci 361(1806):1021–1043
46. Zohdi TI (2017) Dynamic thermomechanical modeling and simulation of the design of rapid free-form 3D printing processes with evolutionary machine learning. Comput Methods Appl Mech Eng. https://doi.org/10.1016/j.cma.2017.11.030
47. Holland JH (1975) Adaptation in natural and artificial systems. University of Michigan Press, Ann Arbor
48. Goldberg DE (1989) Genetic algorithms in search, optimization and machine learning. Addison-Wesley, Boston
49. Davis L (1991) Handbook of genetic algorithms. Thompson Computer Press, Berkeley
50. Onwubiko C (2000) Introduction to engineering design optimization. Prentice Hall, Upper Saddle River
51. Lagaros N, Papadrakakis M, Kokossalakis G (2002) Structural optimization using evolutionary algorithms. Comput Struct 80:571–589
52. Papadrakakis M, Lagaros N, Thierauf G, Cai J (1998a) Advanced solution methods in structural optimisation using evolution strategies. Eng Comput J 15(1):12–34
53. Papadrakakis M, Lagaros N, Tsompanakis Y (1998b) Structural optimization using evolution strategies and neutral networks. Comput Methods Appl Mech Eng 156(1):309–335
54. Papadrakakis M, Lagaros N, Tsompanakis Y (1999a) Optimization of large-scale 3D trusses using Evolution Strategies and Neural Networks. Int J Space Struct 14(3):211–223
55. Papadrakakis M, Tsompanakis J, Lagaros N (1999b) Structural shape optimisation using evolution strategies. Eng Optim 31:515–540
56. Goldberg DE, Deb K (2000) Special issue on Genetic Algorithms. Comput Methods Appl Mech Eng 186(2–4):121–124
57. Thomas D (2017) Could 3D bioprinted tissues offer future hope for microtia treatment? Int J Surg 32:43–44
58. Nakashima Yasuharu, Okazak Ken, Nakayama Koichiet, Okada Seiji, Mizu-uchi Hideki (2017) Bone and joint diseases in present and future. Fukuoka Igaku Zasshi = Hukuoka Acta Medica 108:1–17 (ISSN 0016-254X. PMID 29226660)
59. Doyle Ken (2014) Bioprinting from patches to parts. Gen Eng Biotechnol News 34(10):1–345. https://doi.org/10.1089/gen.34.10.02
60. Boland T, Wilson WC Jr., Xu T (2006) Ink-jet printing of viable cells. US patent 7051654, issued 2006-05-30
61. Shafiee A, Atala A (2016) Printing technologies for medical applications. Trends Mol Med 22(3):254265. https://doi.org/10.1016/j.molmed.2016.01.003
62. Ozbolat IT (2015) Bioprinting scale-up tissue and organ constructs for transplantation. Trends Biotechnol 33(7):395400. https://doi.org/10.1016/j.tibtech.2015.04.005
63. Chua CK, Yeong WY (2015) Bioprinting: principles and applications. World Scientific Publishing Co, Singapore, p 296 (ISBN 9789814612104. Retrieved 17 February 2016)
64. Harmon K (2013) A sweet solution for replacing organs (PDF). Sci Am 308(4):5455. https://doi.org/10.1038/scientificamerican0413-54. (Retrieved 17 February 2016)
65. Murphy S, Atala A (2014) 3D bioprinting of tissues and organs. Nat Biotechnol 32:77385. https://doi.org/10.1038/nbt.2958 PMID 25093879
66. Crawford M (2013) Creating valve tissue using 3-D bioprinting. ASME.org. American Society of Mechanical Engineers, New York (Retrieved 17 February 2016)
67. Murphy SV, Skardal A, Atala A (2013) Evaluation of hydrogels for bio-printing applications. J Biomed Mater Res Part A 101A(1):27284. https://doi.org/10.1002/jbm.a.34326. (PMID 22941807)
68. Souza GR (2010) Three-dimensional tissue culture based on magnetic cell levitation. Nat Nanotechnol 5:2916
69. Haisler WL (2013) Three-dimensional cell culturing by magnetic levitation. Nat Protoc 8:19409
70. Friedrich J, Seidel C, Ebner R, Kunz-Schughart LA (2009) Spheroid-based drug screen: considerations and practical approach. Nat Protoc 4:30924
71. Seiler AEM, Spielmann H (2011) The validated embryonic stem cell test to predict embryotoxicity in vitro. Nat Protoc 6:96178
72. Tseng H (2013) Assembly of a three-dimensional multitype bronchiole coculture model using magnetic levitation. Tissue Eng Part C Methods 19:66575
73. Tseng H (2014) A three-dimensional co-culture model of the aortic valve using magnetic levitation. Acta Biomater 10:17382

74. Daquinag AC, Souza GR, Kolonin MG (2013) Adipose tissue engineering in three-dimensional levitation tissue culture system based on magnetic nanoparticles. Tissue Eng Part C Methods 19:33644
75. Timm DM (2013) A high-throughput three-dimensional cell migration assay for toxicity screening with mobile device-based macroscopic image analysis. Sci Rep 3:3000
76. Gwathmey JK, Tsaioun K, Hajjar RJ (2009) Cardionomics: a new integrative approach for screening cardiotoxicity of drug candidates. Expert Opin Drug Metab Toxicol 5:64760
77. Feynman RP, Leighton RB, Sands M (2006) The Feynman lectures on physics 2. ISBN 0-8053-9045-6
78. Cullity CD, Graham (2008) Introduction to magnetic materials, 2nd edn. Wiley-IEEE Press, New York, p 103 0-471-47741-9
79. Boyer Timothy H (1988) The force on a magnetic dipole. Am J Phys 56(8):688692. https://doi.org/10.1119/1.15501 (Bibcode:1988AmJPh.56.688B)
80. Zienkiewicz OC (1984) Coupled problems & their numerical solution. In: Lewis RW, Bettes P, Hinton E (eds) Numerical methods in coupled systems. Wiley, Chichester, pp 35–58
81. Zienkiewicz OC, Paul DK, Chan AHC (1988) Unconditionally stable staggered solution procedure for soil–pore fluid interaction problems. Int J Numer Methods Eng 26:1039–1055
82. Lewis RW, Schrefler BA, Simoni L (1992) Coupling versus uncoupling in soil consolidation. Int J Numer Anal Methods Geomech 15:533–548
83. Lewis RW, Schrefler BA (1998) The finite element method in the static and dynamic deformation and consolidation of porous media, 2nd edn. Wiley press, New York
84. Park KC, Felippa CA (1983) Partitioned analysis of coupled systems. In: Belytschko T, Hughes TJR (eds) Computational methods for transient analysis. North-Holland, Amsterdam, pp 157–219
85. Farhat C, Lesoinne M, Maman N (1995) Mixed explicit/implicit time integration of coupled aeroelastic problems: three-field formulation, geometric conservation and distributed solution. Int J Numer Methods Fluids 21:807–835
86. Farhat C, Lesoinne M (2000) Two efficient staggered procedures for the serial and parallel solution of three-dimensional nonlinear transient aeroelastic problems. Comput Methods Appl Mech Eng 182:499–516
87. Farhat C, van der Zee G, Geuzaine P (2006) Provably second-order time-accurate loosely-coupled solution algorithms for transient nonlinear computational aeroelasticity. Comput Methods Appl Mech Eng 195:1973–2001
88. Piperno S (1997) Explicit/implicit fluid/structure staggered procedures with a structural predictor & fluid subcycling for 2D inviscid aeroelastic simulations. Int J Numer Methods Fluids 25:1207–1226
89. Piperno S, Farhat C, Larrouturou B (1995) Partitioned procedures for the transient solution of coupled aeroelastic problems—part I: model problem, theory, and two-dimensional application. Comput Methods Appl Mech Eng 124(1–2):79–112
90. Piperno S, Farhat C (2001) Partitioned procedures for the transient solution of coupled aeroelastic problems—part II: energy transfer analysis and three-dimensional applications. Comput Methods Appl Mech Eng 190:3147–3170
91. Michopoulos G, Farhat C, Fish J (2005) Survey on modeling and simulation of multiphysics systems. J Comput Inf Sci Eng 5(3):198–213
92. Lesoinne M, Farhat C (1998) Free staggered algorithm for nonlinear transient aeroelastic problems. AIAA J 36(9):1754–1756
93. Le Tallec P, Mouro J (2001) Fluid structure interaction with large structural displacements. Comput Methods Appl Mech Eng 190(24–25):3039–3067
94. Frenklach M, Carmer CS (1999) Molecular dynamics using combined quantum & empirical forces: application to surface reactions. Adv Class Traject methods 4:27–63
95. Haile JM (1992) Molecular dynamics simulations: elementary methods. Wiley, New York
96. Hase WL (1999) Molecular dynamics of clusters, surfaces, liquids, & interfaces. Advances in classical trajectory methods, vol 4. JAI Press, Stamford
97. Rapaport DC (1995) The art of molecular dynamics simulation. Cambridge University Press, Cambridge
98. Schlick T (2000) Molecular modeling & simulation. An interdisciplinary guide. Springer, New York
99. Moelwyn-Hughes EA (1961) Physical chemistry. Pergamon Press, New York
100. Tersoff J (1988) Empirical interatomic potential for carbon, with applications to amorphous carbon. Phys Rev Lett 61:2879–2882
101. Stillinger FH, Weber TA (1985) Computer simulation of local order in condensed phases of silicon. Phys Rev B 31:5262–5271